Original Paper

A multi-mechanism numerical simulation model for CO_2-EOR and storage in fractured shale oil reservoirs

Yuan-Zheng Wang [a], Ren-Yi Cao [a, *], Zhi-Hao Jia [a], Bin-Yu Wang [a], Ming Ma [b], Lin-Song Cheng [a]

[a] College of Petroleum Engineering, China University of Petroleum (Beijing), Beijing, 102249, China
[b] John & Willie Leone Department of Energy & Mineral Engineering, The Pennsylvania State University, University Park, 16802, PA, USA

A R T I C L E   I N F O

A B S T R A C T

Under the policy background and advocacy of carbon capture, utilization, and storage (CCUS), CO_2-EOR has become a promising direction in the shale oil reservoir industry. The multi-scale pore structure distribution and fracture structure lead to complex multiphase flow, comprehensively considering multiple mechanisms is crucial for development and CO_2 storage in fractured shale reservoirs. In this paper, a multi-mechanism coupled model is developed by MATLAB. Compared to the traditional Eclipse 300 and MATLAB Reservoir Simulation Toolbox (MRST), this model considers the impact of pore structure on fluid phase behavior by the modified Peng−Robinson equation of state (PR-EOS), and the effect simultaneously radiate to Maxwell−Stefan (M−S) diffusion, stress sensitivity, the nano-confinement (N-C) effect. Moreover, a modified embedded discrete fracture model (EDFM) is used to model the complex fractures, which optimizes connection types and half-transmissibility calculation approaches between non-neighboring connections (NNCs). The full implicit equation adopts the finite volume method (FVM) and Newton−Raphson iteration for discretization and solution. The model verification with the Eclipse 300 and MRST is satisfactory. The results show that the interaction between the mechanisms significantly affects the production performance and storage characteristics. The effect of molecular diffusion may be overestimated in oil-dominated (liquid-dominated) shale reservoirs. The well spacing and injection gas rate are the most crucial factors affecting the production by sensitivity analysis. Moreover, the potential gas invasion risk is mentioned. This model provides a reliable theoretical basis for CO_2-EOR and sequestration in shale oil reservoirs.

1. Introduction

CCUS is an extension of the carbon capture and storage (CCS) concept and technology (ICF International, 2010). CCS refers to the process of CO_2 capture from emission sources and energy industries and storage in geological structures. CCS concept and technology development is divided into four stages: concept, formation, application, and promotion (Wang, 2023). Although CCS is deemed the key reserve technology for addressing climate change, the technology does not consider the economic return after operation, which restricts the development of CCS technology to a certain extent. China emphasizes and advocates the concept of CCUS, emphasizing the rational and effective utilization. This concept is widely accepted and applied in the reservoir industry, which further guarantees the sustainable development of traditional fossil energy industries. CCS/CCUS technologies are committed to mitigating the greenhouse effect and creating a sustainable and low-carbon society (IEA, 2017; Zhang et al., 2020; Wang et al., 2022). This process, affected by economic, technological, and quantitative constraints, will be promising and challenging work (Bui et al., 2018; IEA, 2020, 2021).

The CO_2-EOR is deemed a promising potential direction of CCUS strategy in the oil industry (Jia et al., 2019). Some unique mechanisms, such as adsorption, diffusion, and miscible phase, have been widely studied through physical simulation experiments as the theoretical basis for CO_2 storage and utilization, and these effects are further amplified at ultra-tight shale reservoirs (Curtis, 2002; Ma, 2018; Zhang et al., 2019). Meanwhile, the interaction between

* Corresponding author.
  E-mail address: caorenyi@126.com (R.-Y. Cao).

CO_2 and reservoir rocks enhances the seepage capacity of fluid (Steven et al., 2013; Chi et al., 2017). Under the conventional pressure−volume−temperature (PVT) experiment, CO_2 mixed with oil had the least minimum miscibility pressure (MMP) and a noticeable effect in viscosity reduction through all injection gas tests (Luo et al., 2017; Hashemi and Sedaee, 2022), this effect will be more significant in nanopores (Song Z.J. et al., 2020). The phase behavior of fluid in nanopores will be shifted, which will further lead to the change of fluid properties, these phenomena are captured in the simulation processes of grand canonical Monte Carlo (GCMC) (Morishige et al., 1997; Singh et al., 2009; Singh and Singh, 2011). A series of modifications for traditional EOS with pore-size-dependent forms were proposed to expect a more accurate prediction of phase behavior in confined space (Sanaei et al., 2014; Khanal et al., 2021). Furthermore, the interphase capillary pressure and adsorption mechanisms were considered in subsequent work (Song Y.L. et al., 2020a, 2020b), which provided the theoretical bases for CO_2-EOR of shale reservoirs.

Modeling of natural and hydraulic fractures is necessary for shale reservoirs. Some traditional approaches use local grid refinement (LGR) with unstructured meshes to model fractures, such as the discrete fracture model (DFM) (Sandve et al., 2012; Hui et al., 2013), but meshing and computing are extremely time-consuming. The EDFM was developed to improve the computational efficiency in the condition of complex multiscale fractures (Li and Lee, 2008). The structured mesh is used to simulate the orthogonal matrix mesh without considering the complex fracture cells, and the fracture with complex orientation and geometric shape communicates with the matrix mesh through NNCs. These approaches have a significant advantage in dealing with massive multiscale fractures and are successfully applied to developing fractured shale reservoirs (Moinfar et al., 2014; Xu et al., 2017). Due to unreasonable allocation rules between the NNCs, EDFM cannot apply the condition of the fracture with small permeability and reservoirs with impermeable flow barriers (Zhang et al., 2017). The projection-based EDFM (pEDFM) was developed by Țene et al. (2017), this approach overcomes the limitation of EDFM by modifying the allocation of flow flux between NNCs. In subsequent works, the researchers extended the pEDFM by considering additional connections and conductivity modification (Cao et al., 2019; Rao et al., 2020, 2022; Olorode et al., 2020).

Currently, CO_2-EOR and storage, as an integral whole, are widely mentioned in numerical simulation (Sanchez-Rivera et al., 2015; Zhao et al., 2018; Eyinla et al., 2023; Wan et al., 2023). Although the importance of multiple mechanisms in shale reservoirs has been proved by numerical simulations, such as diffusion and adsorption (Yanze and Clemens, 2012; Bao et al., 2018; Zhao X.R. et al., 2023), this conclusion is unacceptable because the oil (liquid phase) is not the dominant phase in their study. In oil-dominated shale reservoirs, the contribution of diffusion to production and CO_2 storage in the presence of gas only in the SRV region needs to be further evaluated. Meanwhile, unlike water flooding of conventional reservoirs, the response time of gas injection is longer in ultra-tight reservoirs, which leads to the economic rate of return being unacceptable in the short term. The natural depletion of development is commonly used in the actual field. Under the current CCUS advocacy and policy, CO_2 storage and utilization has become an important indicator in reservoir development. Although CO_2-cycling huff and puff operation is a promising approach for shale reservoirs, the captured CO_2 amount is limited, and this approach has not widely gained field adoption due to vague understandings in several aspects (Fragoso et al., 2018). CO_2 flooding is still promising, significantly improving oil recovery and storage. However, this preliminary understanding needs further research and verification, which is the purpose of this paper.

Based on the abovementioned problems, this paper proposed a fully coupled numerical simulation model considering multiple mechanisms, such as the N-C effect, stress sensitivity, and molecular diffusion, to evaluate the production performance and CO_2 storage characteristics during CO_2-EOR in shale reservoirs. pEDFM was used to model complex fractures. In Section 2, the details of the model are presented, mainly including the modeling of multiple mechanisms, the modified PR-EOS, the connection types and expression of the mass transfer between NNCs in pEDFM, and the discretization and solution of the governing equation. Section 3 is model validation and mechanisms analysis. Section 4 discusses the sensitivity of the reservoir and production parameters on production and CO_2 storage. Section 5 is the conclusion of the paper.

2. Methodology

2.1. Physical model and assumption

Fig. 1 shows the multistage fractured shale reservoir model. The stimulated reservoir volume (SRV) contains 15 hydraulic fracturing fractures and natural fractures with different half-lengths. Natural fractures are randomly generated in the model. There are four vertical injection wells in the corners and a horizontal well in the center of the model, and the well pattern model refers to the typical ultra-tight reservoir (Zhao et al., 2015). The fractures are modeled using modified EDFM with unstructured grids. More details of pEDFM will be found in Section 2.2.3.

The following assumptions are proposed to ensure the accuracy of multi-mechanism coupling modeling and computational efficiency.

(1) The reservoir maintains a constant temperature environment to avoid complicated modeling work considering the non-isothermal system.
(2) The reservoir fluid contains oil phase, gas phase, and water phase. Fluid transport is contributed by advection and molecular diffusion; and advection satisfies Darcy's law.
(3) The phase equilibrium only considers the oil and gas phases, and the mass transfer instantaneously achieves phase equilibrium.
(4) Neglecting hydrocarbon dissolution and escape processes in the water phase. Only oil and gas phases are considered in phase equilibrium calculations due to suitability of classical
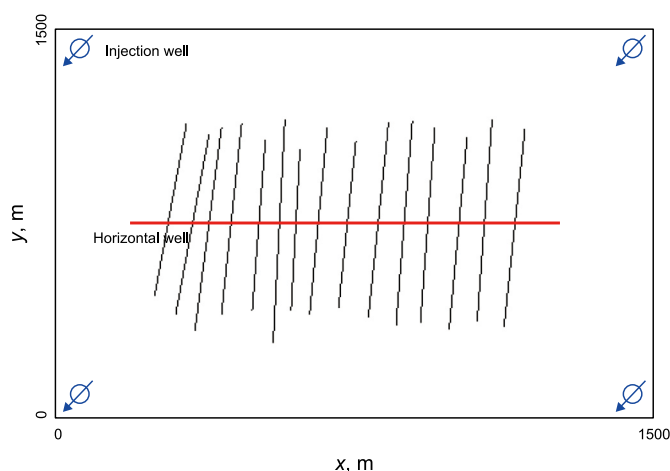

Fig. 1. Physical model in this paper.

van der Waals mixing rules in PR−EOS (Huron and Vidal, 1979; Lindeloff and Michelsen, 2003).

(5) The molecular diffusion of the water phase is not considered.

(6) To simplify the connection between meshes and the conductivity calculation, hydraulic fractures penetrate shale formations without interfering with each other.

2.2. Mathematical model

2.2.1. Mass governing equation

A mass-conservation governing equation coupled with advection and diffusion transport was proposed. In Eq. (1), each term from left to right is the mass term, advection term, diffusion term, well source, and non-adjacent connected flow rate.

$$
\frac{\partial}{\partial t}\left[\phi \sum_{\alpha=\text{L,V}} \left(\rho_\alpha S_\alpha X_{\alpha,i}\right)\right] + \nabla \cdot \left(\sum_{\alpha=\text{L,V}} \rho_\alpha \overrightarrow{v}_\alpha X_{\alpha,i}\right) + J_{\alpha,i}
$$
$$
- \left(\sum_{\alpha=\text{L,V}} q_{\alpha,i}^{\text{well}} - q_{\alpha,i}^{\text{nnc}}\right)/V_{\text{cell}} = 0
\tag{1}
$$

The mass-conservation governing equation of aqueous phase is as follows:

$$
\frac{\partial}{\partial t}(\phi \rho_{\text{w}} S_{\text{w}}) + \nabla \cdot \left(\rho_{\text{w}} \overrightarrow{v}_{\text{w}}\right) - \left(q_{\text{w}}^{\text{nnc}} - q_{\text{w}}^{\text{well}}\right)/V_{\text{cell}} = 0
\tag{2}
$$

where subscripts L, V, and w represent liquid phase, vapor phase, and aqueous phase, respectively; α refers to the phase ($\alpha = $ L, V); i represents the component i; $X_{\alpha,i}$ is the mole fraction of component i in phase α; ϕ is the porosity; S is the saturation; v and ρ are the velocity and density; q^{nnc} is the total flow flux between NNCs; q^{well} is the source term of well; V_{cell} is the volume of cell.

The velocity of each phase by Darcy's law is given by

$$
\overrightarrow{v}_\alpha = -\frac{KK_{\text{r},\alpha}(S)}{\mu_\alpha}(\nabla P_\alpha - \rho_\alpha g \nabla z) = -K\lambda_\alpha(\nabla P_\alpha - \rho_\alpha g \nabla z)
\tag{3}
$$

where K is the absolute permeability; K_{r} is the relative permeability; μ is the viscosity; g is the gravity constant; ∇z is the gravity gradient.

2.2.2. M−S diffusion model

In this paper, M−S diffusion is used to describe the mechanism of multi-component transport in shale reservoirs (Tian et al., 2021). In an isothermal system, the most comprehensive form is written as

$$
-\frac{c_i x_i}{RT}\nabla\mu_i = \sum_{\substack{j=1\\j\neq i}}^{N_c} \frac{x_j J_i - x_i J_j}{D_{i,j}}
\tag{4}
$$

where c_i is the molar concentration of component i; x_i is the mole fraction of component i; x_j the mole fraction of component j; $\nabla\mu$ is the chemical potential gradient; $D_{i,j}$ is the binary pair i-j diffusion coefficient; R is the ideal gas constant; T is the temperature; J is the diffusion flux; N_c is the number of components.

With equimolar constraint, the multi-component flow flux can be written in matrix form:

$$
J = -\frac{C_t}{RT}B^{-1}X\nabla\mu
\tag{5}
$$

The elements of matrix B are the function of the M−S diffusion coefficient and mole fraction. The relationship between chemical potentials and fugacities is given by

$$
\mu_i = \mu_{\text{ref}} + RT\ln\left(f_i \big/ f_{i,\text{ref}}\right)
\tag{6}
$$

where superscript ref refers to the reference state; f is the fugacity. The chemical potential gradient is converted to the function of fugacity and component:

$$
\nabla\mu_i = RT \sum_{j=1}^{N_c-1} \frac{\partial\ln(f_i)}{\partial x_j}\nabla x_j
\tag{7}
$$

Substituting Eqs. (6) and (7) into Eq. (5), we obtain the flow flux by molecular diffusion. In the porous medium the flow flux can be further affected by porosity ϕ, phase saturation S, and tortuosity τ and can be expressed as follows:

$$
J = -\rho\frac{\phi S}{\tau}B^{-1}X\nabla\ln f
\tag{8}
$$

The elements of matrix B are given by the following formula:

$$
B_{i,j} = \begin{cases} \displaystyle\sum_{j\neq i}^{N_c} \frac{x_j}{D_{i,j}} + \frac{x_i}{D_{i,N_c}}, & i=j \\[4mm] \displaystyle\frac{x_i}{D_{i,N_c}} - \frac{x_i}{D_{i,j}}, & i\neq j \end{cases}
\tag{9}
$$

Due to sparse experimental data and experimental uncertainty interference, it is different to predict the diffusion coefficients of multi-component mixtures. The binary infinite dilution coefficients are commonly used to predict the elements of the M−S diffusion coefficient matrix (Vignes, 1966). In an infinite diluted solution, molecular diffusion coefficients (a binary pair i-j) become equal for the given multi-component. The generalized Vignes relation is the most comprehensive approach to estimating the M−S diffusion coefficient, which is given by

$$
D_{i,j} = \left(D_{i,j}^\infty\right)^{x_j}\left(D_{j,i}^\infty\right)^{x_i}\prod_{\substack{k=1\\k\neq i,j}}^{N_c}\left(D_{i,k}^\infty D_{j,k}^\infty\right)^{x_k/2}
\tag{10}
$$

where $D_{i,j}^\infty$ is the diffusion coefficient of component i diluted in solvent j. A correlation relation is proposed to describe the above diffusion coefficient by physical properties and thermodynamic parameters of fluids (Leahy-Dios and Firoozabadi, 2007). More details can be found in the published literature (Fuller et al., 1966, 1969).

2.2.3. Mass transfer between NNCs in pEDFM

pEDFM was developed by modifying the EDFM, which can realize the modeling of complex fractured reservoirs. The connection types in pEDFM are introduced in Fig. 2. There are six types of connection relationships: (I) adjacent matrix cells (M_1 and M_2), (II) adjacent fracture cells within an individual fracture (F_1 and F_2), (III) the connection between different fracture cells in the same matrix mesh (F_3 and F_4), (IV) the matrix and fracture cell ($F_{1,3,4}$ with M_1 or $F_{2,5}$ with M_2), (V) the connection between fractures in adjacent matrix meshes ($F_{1,3,4}$ with F_5 or F_2 with $F_{3,4}$), and (VI) the fracture cell with adjacent matrix cell ($F_{1,3,4}$ with M_2 or $F_{2,5}$ with M_1) (Jiang and Younis, 2017; Cao et al., 2019; Rao et al., 2020, 2022; Olorode et al., 2020).

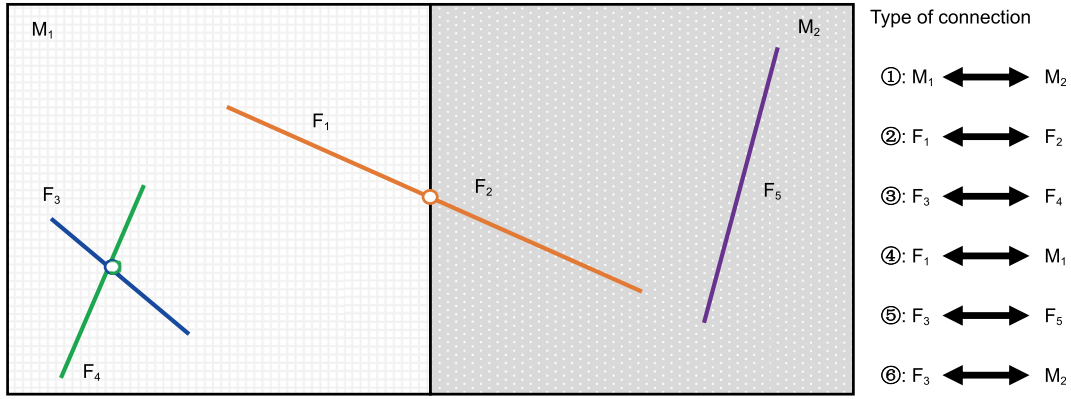**Fig. 2.** Connection types in pEDFM.

In previous studies, the expression of the flow flux between NNCs is similar to Darcy's law and is given by

$$q_{\alpha,i}^{nnc} = \sum_{m=1}^{N_{nnc}} G_m \sum_{\alpha=1}^{N_p} \lambda_\alpha \rho_{\alpha,m} X_{\alpha,i}(P_\alpha - P_{\alpha,m}) \tag{11}$$

where N_{nnc} is the number of adjacent cells communicated by NNC; N_p is the total number of phases; λ is the phase mobility; G_m is the convection-dominated transmissibility factor, which is a function of geometry and absolute permeability. The flow flux between matrix cells was calculated using standard methods, which are also applicable between fracture cells. More details can be found in previous studies (Moinfar et al., 2014; Xu et al., 2019; Yu et al., 2018). For example, the convection-dominated transmissibility factor G_{M_1,F_1} between matrix and fracture cell (M_1 with F_1) is given by

$$G_{M_1,F_1} = \left[G_{M_1}^{-1} + G_{F_1}^{-1}\right]^{-1}, \quad G_{M_1} = \frac{A_{M_1,F_1}k_{M_1}}{\langle d_{M_1,F_1}\rangle}, \quad G_{F_1} = \frac{A_{M_1,F_1}k_{F_1}}{w_{F_1}} \tag{12}$$

where $A_{M_1F_1}$ is the effective contact area between M_1 and F_1; $\langle d_{M_1F_1}\rangle$ is the distance between the center of the matrix M_1 and the center of the fracture F_1; w_{F_1} is the width of fracture. Although the diffusion was modeled through the M−S method, the flow flux only considers the convection term derived by the pressure gradient between NNCs (Olorode et al., 2021). As shown in Eq. (13), the expression of the total flow is extended by adding the diffusion-dominated term in this paper. In addition, the diffusion-dominated transmissibility factor is defined as the following equation (Eq. (14)). The expression is similar to the traditional transmissibility factor. In all types of connections, the permeability only needs to be replaced by B^{-1}.

$$\begin{aligned} q_{\alpha,i}^{nnc} = &\sum_{m=1}^{N_{nnc}} G_m \sum_{\alpha=1}^{N_p} \lambda_\alpha \rho_{\alpha,m} X_{\alpha,i}(P_\alpha - P_{\alpha,m}) \\ &+ \sum_{m=1}^{N_{nnc}} \sum_{\alpha=1}^{N_p} T_{\alpha,m}\rho_{\alpha,m} X_{\alpha,i}\left\{-\frac{\phi_m S_{\alpha,m}}{\tau}\left(\ln f_{\alpha,i} - \ln f_{\alpha,m,i}\right)\right\} \end{aligned} \tag{13}$$

$$T_{\alpha,m} = \frac{(B_{\alpha,m})^{-1}A_{nnc}}{d_{nnc}} \tag{14}$$

2.2.4. Phase equilibrium calculation of mixtures in nanopores

The phase behavior of fluid in nanopores will be shift, which significantly affects the distribution of vapor and liquid phases, the phenomenon has been captured by molecular simulations (Zarragoicoechea and Kuz, 2004). This paper considers the shift of the critical parameters related to the pore-throat radius proposed by GCMC simulation as follows:

$$\Delta P_c^* = \frac{P_{cb} - P_{cp}}{P_{cb}} = 0.9409(\sigma_{LJ}/r) - 0.2415(\sigma_{LJ}/r)^2 \tag{15}$$

$$\Delta T_c^* = \frac{T_{cb} - T_{cp}}{T_{cb}} = 0.9409(\sigma_{LJ}/r) - 0.2415(\sigma_{LJ}/r)^2 \tag{16}$$

where subscripts cb and cp represent the bulk and confined space, respectively; ΔP_c^* and ΔT_c^* are relative shifts of critical parameters; r is the pore-throat radius; δ_{LJ} is the Lennard-Jones size parameter.

Phase equilibrium of mixture needs to satisfy.

$$\sum_{i=1}^{N_c} z_i = \sum_{i=1}^{N_c} x_i = \sum_{i=1}^{N_c} y_i = 1 \tag{17}$$

$$S_w + S_o + S_g = 1 \tag{18}$$

$$f_{L,i}(P_L, x_i) = f_{V,i}(P_L + P_{cap}, y_i), \quad i = 1, 2, ..., N_c \tag{19}$$

In addition, interphase pressure becomes significant in nanopores, and capillary pressure P_{cap} between liquid and gas phases is given by Eq. (20) (Adamson, 1990).

$$P_{cap} = P_V - P_L = \frac{2\sigma\cos\theta}{r} \tag{20}$$

where σ is the interfacial tension; θ is the contact angle. The interfacial tension is estimated using the Parachor model:

$$\sigma = \left[\sum_i^{N_c} \left(\rho_L[P]_i x_i - \rho_V[P]_i y_i\right)\right]^\upsilon \tag{21}$$

where υ is the exponent; $[P]$ is the Parachor parameter of the pure component. The vapor−liquid equilibrium is calculated by the Rachford−Rice (R−R) correlation formula (Rachford and Rice, 1952):

$$\sum_{i=1}^{N_c} \frac{(K_i - 1)z_i}{1 + F_V(K_i - 1)} = 0 \tag{22}$$

where F_V is the mole fraction of the vapor phase; K is the equilibrium coefficient related to the fugacity coefficient, which is automatically updated through the iteration. Fig. 3 shows the flow chart of phase equilibrium, the corresponding equations are labeled in the figure, and the output results are also used to calculate the M–S diffusion coefficient. The phase behavior calculation based on the pore scale is used to couple multiple mechanisms, such as M–S diffusion and Darcy's flow, further strengthening the control of the pore scale on fluid transport. Compared with previous studies, this modeling method is more suitable for the multi-scale seepage environment in shale reservoirs.

2.2.5. Stress sensitivity of porous media

The stress sensitivity of the shale reservoirs will lead to the loss of permeability, which will lead to deviations in the assessment of reservoir production performance, this condition has been observed in many experiments with shale samples. A conceptual model called 'bed of nails', was proposed by Gangi to capture the stress dependence of the slit-shaped pore. In this paper, Gangi's model was used to capture the stress dependence of matrix pore (Gangi, 1978; Wasaki and Akkutlu, 2015):

$$K_f = K_o \left[1 - \left(\frac{P_c - \sigma_\alpha p}{P_{max}} \right)^m \right]^3 \tag{23}$$

where σ_α is Biot's constant; P_c is the confining stress; P_{max} is the maximum stress when the fracture is closed; K_o is the permeability at zero confining stress; K_f is the current matrix permeability.

2.2.6. Wellbore effects

The wellbore index (WI) between well and fracture connections calculated by the Peaceman model:

$$WI = \frac{2\pi K_f W_f}{\ln\left(r_e / r_f \right)} \tag{24}$$

$$r_e = 0.14\sqrt{L_f^2 + W_f^2} \tag{25}$$

where r_e and r_f are the effective wellbore radius and actual wellbore radius, respectively; W_f is the fracture aperture; L_f and W_f refer to the length and height of the fracture cell.

2.2.7. Discretization and solution of governing equation of compositional model

This section proposes a full-component numerical simulation using pEDFM to model complex fractures. The mass-conservation governing equation for component i is given by

$$\frac{\partial}{\partial t}[\phi(\rho_L S_L x_i + \rho_V S_V y_i)] + \nabla \cdot \left(\rho_L x_i \overrightarrow{v}_L + \rho_V y_i \overrightarrow{v}_V + J_{L,i} + J_{V,i} \right)$$
$$- \left(\rho_L q_{L,i}^{well} + \rho_V q_{V,i}^{well} \right)/V_{cell} + \left(q_{L,i}^{nnc} + q_{V,i}^{nnc} \right)/V_{cell}$$
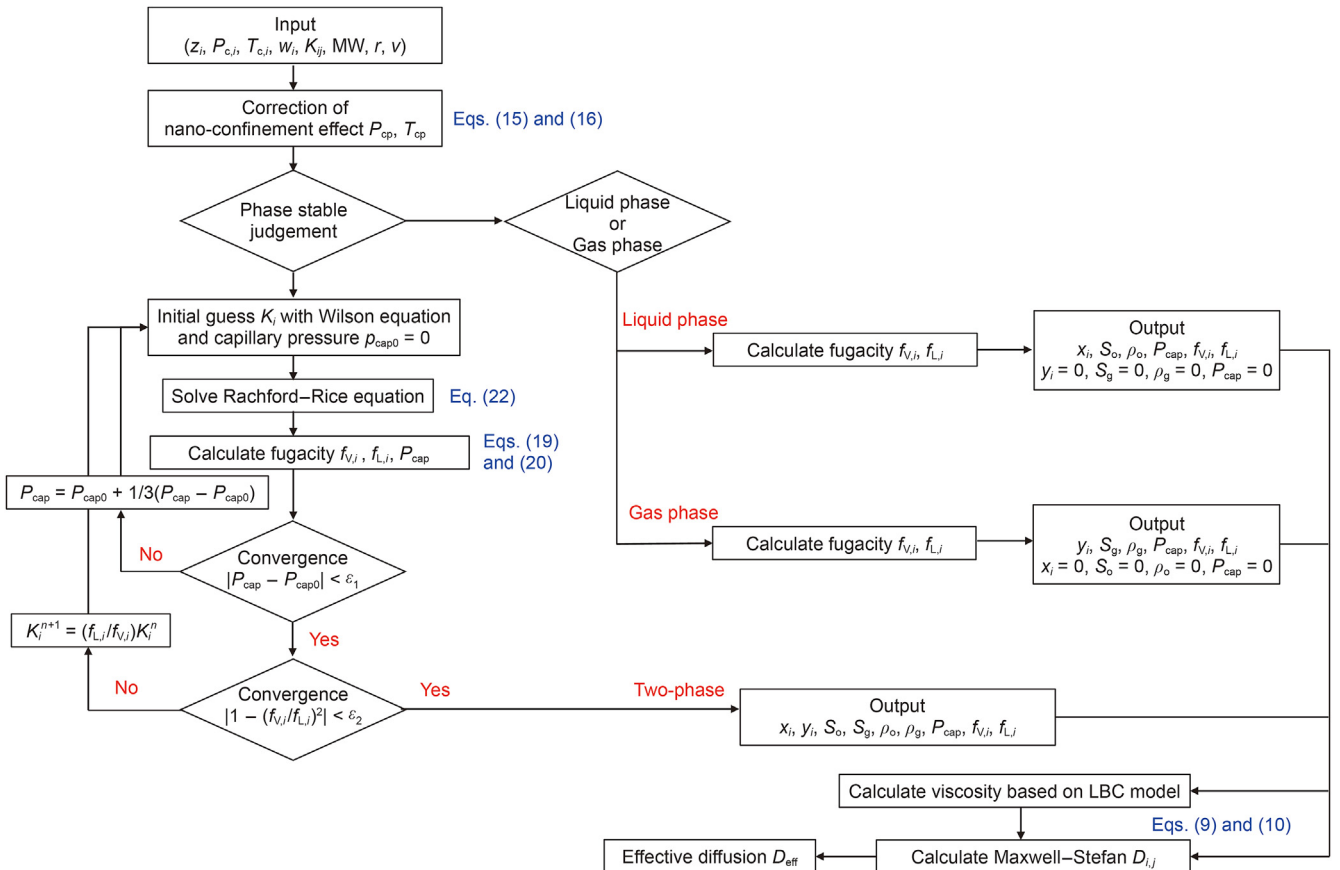$$= 0$$
$$\tag{26}$$

Fig. 3. Flow chart of gas–liquid equilibrium and parameter calculation. The viscosities of the phases were calculated by the Lohrenz–Bray–Clark model (Lohrenz et al., 1964).

The mass-conservation governing equation for the aqueous phase is

$$\frac{\partial}{\partial t}(\phi \rho_{\mathrm{w}} S_{\mathrm{w}}) + \nabla \cdot \left(\rho_{\mathrm{w}} \vec{v}_{\mathrm{w}}\right) - \left(q_{\mathrm{w}}^{\mathrm{well}} - q_{\mathrm{w}}^{\mathrm{nnc}}\right)/V_{\mathrm{cell}} = 0 \qquad (27)$$

The backward Euler scheme and finite-volume method are applied to the temporal discretization and spatial discretization of the equation. In the M−S diffusion equation, the chemical potential gradient in Eq. (4) is given with the premise of constant pressure and temperature. In the numerical simulation, the chemical potential gradient is calculated in adjacent cells. The pressure difference between cells violates the initial assumption in the precondition of the M−S approach. This paper assumes that pressure dependence of the chemical potential between two neighboring cells is ignored when mesh size is within the appropriate range (Moortgat and Firoozabadi, 2013).

The nonlinear equations (Eqs. (28) and (29)) need to be solved by Newton's iteration method. The residual forms of liquid and vapor phases are given by

et al. (2020). Eclipse 300 and MRST are used to verify the model. The MRST is a free open-source software developed by researchers from Heriot-Watt University, which is widely used in reservoir modeling and numerical simulation. Eclipse 300 is a commercial component simulator with a fully implicit solution approach. Fig. 4 shows the reservoir model. A production well is located in the center of the reservoir with gas injection wells on either side. There is an impermeable flow barrier (fracture) with a length of 100 m between the injection and production wells, and that penetrates the whole reservoir. The matrix mesh number is $50 \times 50 \times 2$, the mesh size is $10\ \mathrm{m} \times 10\ \mathrm{m} \times 5\ \mathrm{m}$, the mechanism of diffusion, N-C effect, and stress sensitivity are not considered in the verification model due to model difference, and the fracture is modeled in MRST and Eclipse 300 using pEDFM and the LGR approach, respectively.

In the validation model, the initial reservoir pressure is 27 MPa. The constant reservoir temperature is 135 °C. The matrix permeability is 0.1 mD, and the porosity is 4%. Constant injection and production pressures are 35 and 15 MPa, CO_2 is selected as the injection medium. The pseudo-components and parameters are field data from the Gulong shale reservoir in northern China and are

$$
\begin{aligned}
R_{i,mn}^{t+\Delta t} = & -\sum_{m=1}^{N_{\mathrm{nnc}}} G_{\mathrm{MN}} \left[\rho_{\mathrm{L}} x_i \lambda_{\mathrm{L},mn} \left(P_{\mathrm{L},n} - p_{\mathrm{L},m}\right) + \rho_{\mathrm{V}} y_i \lambda_{\mathrm{V},mn} \left(P_{\mathrm{L},n} - P_{\mathrm{L},m} + P_{\mathrm{cap},n} - P_{\mathrm{cap},m}\right) \right]^{t+\Delta t} \\
& - \sum_{m=1}^{N_{\mathrm{nnc}}} \left(\frac{\phi S_{\mathrm{V}}}{\tau} \rho_{\mathrm{V}} y_i T_{\mathrm{V},mn} \left(\ln f_{i,\mathrm{V},n} - \ln f_{i,\mathrm{V},m}\right) + \frac{\phi S_{\mathrm{L}}}{\tau} \rho_{\mathrm{L}} x_i T_{\mathrm{L},mn} \left(\ln f_{i,\mathrm{L},n} - \ln f_{i,\mathrm{L},m}\right) \right)^{t+\Delta t} - \frac{\Delta V}{\Delta t} \left\{ \left[\phi z_i (S_{\mathrm{L}}\rho_{\mathrm{L}} + S_{\mathrm{V}}\rho_{\mathrm{V}})\right]^{t+\Delta t} \right. \\
& \left. - \left[\phi z_i (S_{\mathrm{L}}\rho_{\mathrm{L}} + S_{\mathrm{V}}\rho_{\mathrm{V}})\right]^{t} \right\} + \left[\rho_{\mathrm{L}} x_i q_{\mathrm{L}}^{\mathrm{well}} + \rho_{\mathrm{V}} y_i q_{\mathrm{V}}^{\mathrm{well}}\right]^{t+\Delta t} + \left[q_{i,\mathrm{V}}^{\mathrm{nnc}} + q_{i,\mathrm{L}}^{\mathrm{nnc}}\right]^{t+\Delta t}
\end{aligned}
$$

$$(28)$$

where subscripts n and m refer to the central grid and adjacent grids; t is the previous time step; Δt is the time increment.

The aqueous phase equation is given by

$$
\begin{aligned}
R_{\mathrm{w},n}^{t+\Delta t} = & -\sum_{m=1}^{N_{\mathrm{nnc}}} \left[G_{nm} \rho_{\mathrm{w}} \lambda_{\mathrm{w},nm} \left(P_{\mathrm{L},n} - P_{\mathrm{L},m}\right)\right]^{t+\Delta t} + \left[q_{\mathrm{w}}^{\mathrm{nnc}}\right]^{t+\Delta t} \\
& + \left[\rho_{\mathrm{w}} q_{\mathrm{w}}^{\mathrm{well}}\right]^{t+\Delta t} - \frac{\Delta V}{\Delta t} \left\{ \left[\phi (S_{\mathrm{w}}\rho_{\mathrm{w}})\right]^{t+\Delta t} - \left[\phi (S_{\mathrm{w}}\rho_{\mathrm{w}})\right]^{t} \right\}
\end{aligned}
$$

$$(29)$$

The partial derivative of the residuals concerning each principal variable is obtained by automatic differential function by MATLAB® (The MathWorks, USA). This paper chooses the total mole fraction of components as the principal variable. In this system, the degree of freedom is $N_{\mathrm{c}} + 1$, the total unknown parameter is $3N_{\mathrm{c}} + 5$, and the principal variables are P_{L}, S_{w}, z_1, z_2, ..., $z_{N_{\mathrm{c}}-1}$. The matrix form using the Newton−Raphson method is given by (Jia et al., 2023)

$$\frac{\partial R^{t+1}}{\partial X} \Delta X = -R^{t+1}(X), \quad \Delta X = \left[P_{\mathrm{L}}, S_{\mathrm{W}}, Z_1, Z_2, ..., Z_{N_{\mathrm{c}}-1}\right] \qquad (30)$$

The automatic differentiation method in MATLAB is used to construct the solution matrix for the Newton−Raphson iteration method. Furthermore, fully implicit equations are used to solve the principal variables.

3. Model validation and analysis

3.1. Model validation

In this paper, we refer to the modeling idea proposed by Olorode

given in Table 1. More parameters and details can be found in the literature (Jia et al., 2023).

Fig. 5 shows profiles of CO_2 mole fractions after 300 and 600 days. Our simulation results demonstrate the advantages of the pEDFM approach compared to the EDFM. When the CO_2 front reaches the barrier, such as a fault, the flow will flow along both sides. Traditional EDFM has abnormal flow characteristics, the phenomenon of fluid passing through the barrier. The model can reproduce the production history of Eclipse 300 and MRST. In addition, Fig. 6 shows comparison results of the cumulative oil production. The simulation results accurately match the Eclipse 300 and MRST, indicating that the model's reliability is satisfactory.

3.2. Mechanism analysis

In order to further analyze the impact of multiple mechanisms on production and CO_2 storage under actual reservoir conditions, including the N-C effect, stress sensitivity, and molecular diffusion, this section simulates the production history and CO_2 storage characteristics considering each mechanism separately and integrated coupled models. The components are extracted oil samples from the Gulong shale reservoir in China. The N_2 adsorption and high-pressure mercury injection experiments of core samples show that the pore size of the matrix is mainly between 10 and 30 nm (Sun et al., 2023; Zhao W.Z. et al., 2023). Pores less than 10 nm account for more than 40 % of the reservoir pore volume (Wang et al., 2023). At the same time, the rich bedding planes further improve the physical properties and storage spaces of the reservoir (Sun et al., 2021). Based on the pore structure distribution and reservoir characteristics, the average pore size is set to 20 nm, the porosity is 6%, and the matrix permeability is 0.01 mD. Fig. 7 reports
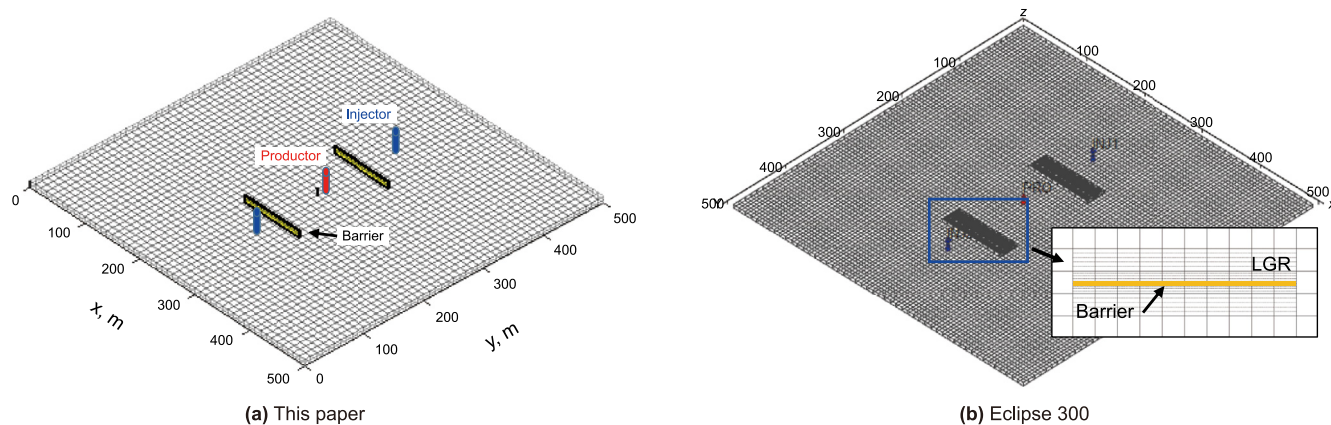
(a) This paper   **(b)** Eclipse 300

Fig. 4. Reservoir models based on this paper and Eclipse 300.

Table 1
Pseudo-components and parameters used for model validation and subsequent section.

Pseudo-component	Mole fraction, %	Critical temperature, K	Critical pressure, MPa	Acentric factor	Critical volume, 10^3 m^3/mol	Molecular weight, g/mol	Parachor parameter, nm
N_2	1.86	126.20	3.46	0.038	0.089	28.01	41.00
CO_2	3.98	304.19	7.38	0.228	0.094	44.01	26.90
C_1	54.85	190.56	4.60	0.012	0.099	16.04	16.00
C_2-C_5	23.55	352.09	4.45	0.135	0.183	40.07	52.12
C_6-C_{10}	4.59	582.04	2.81	0.322	0.434	111.18	142.28
C_{11+}	11.17	761.26	1.59	0.623	0.955	243.66	820.42

(a) The model   **(b)** MRST   **(c)** Eclipse 300
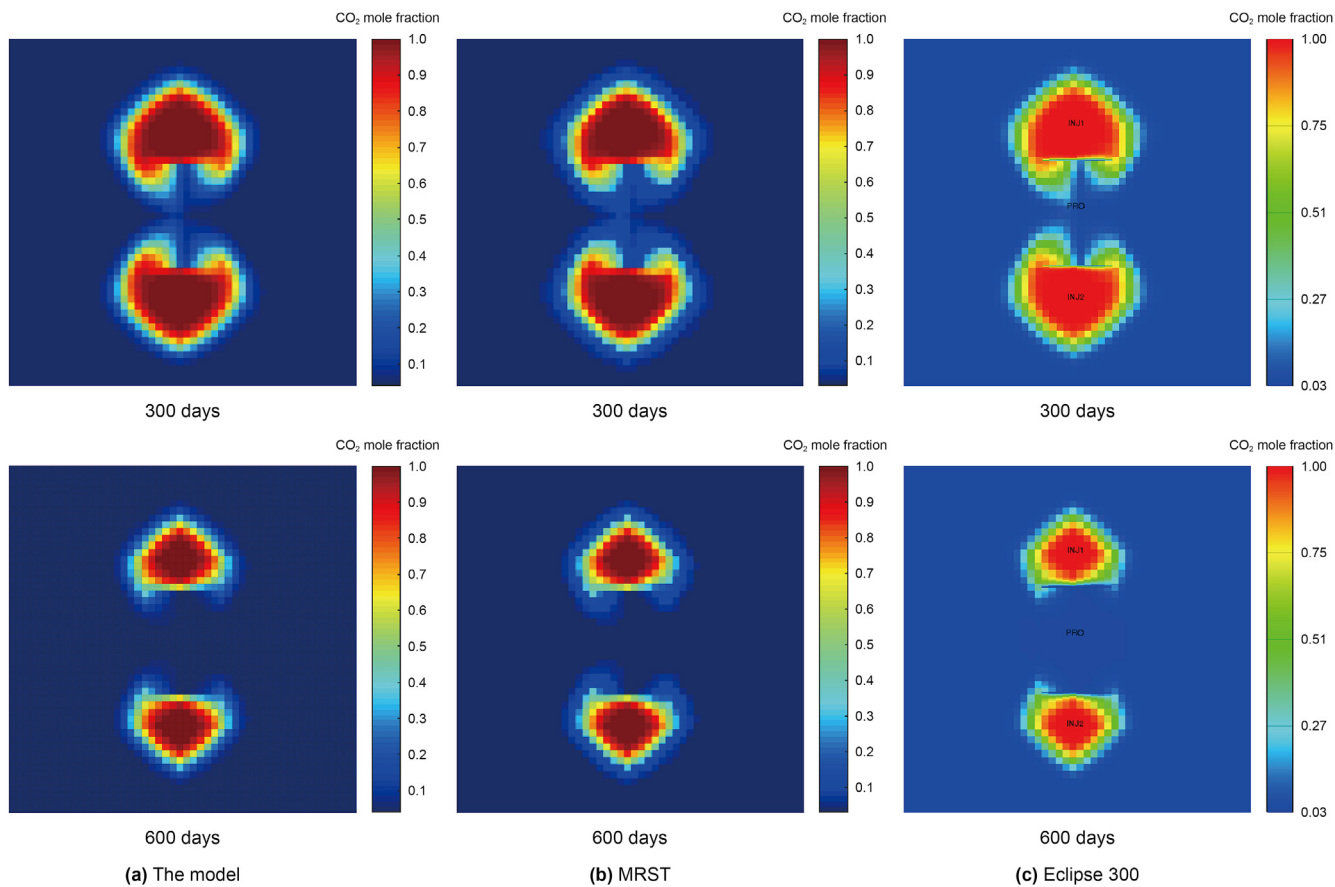
Fig. 5. CO_2 mole fractions at the 300 and 600 days of production.
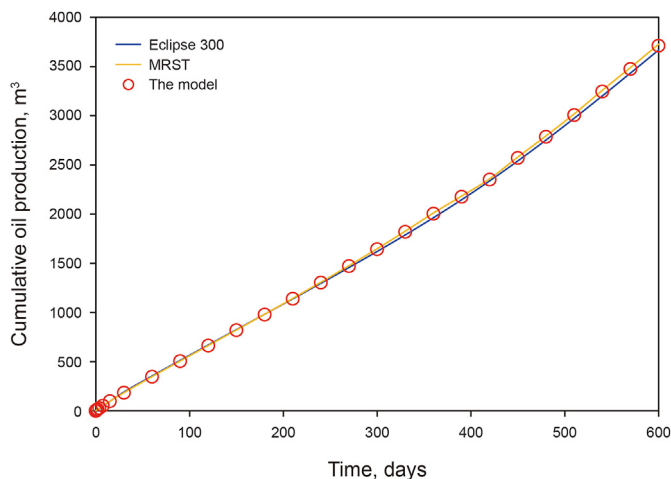
Fig. 6. Cumulative oil production of the verification case.
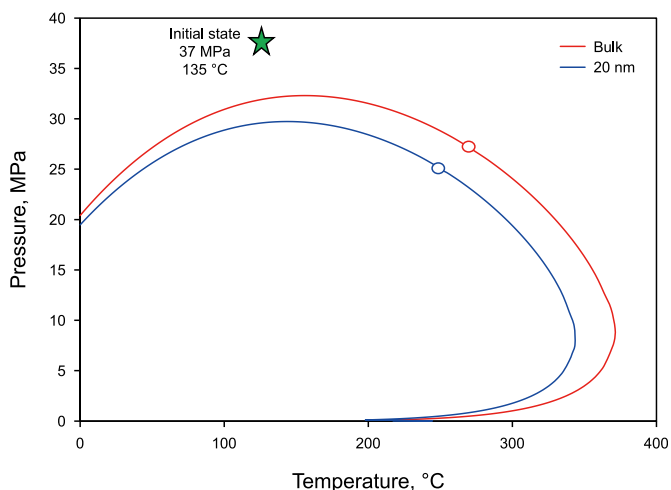
Fig. 7. Phase envelope of mixture in confined and bulk space.

the phase envelope of the initial components in confined and bulk space, the phase envelope shrinks inward, and the bubble point pressure decreases after considering the N-C effect, which has been confirmed in previous research (Wang et al., 2023).

Reservoir model is shown in Fig. 1, and the basic reservoir parameters are listed in Table 2. The value of tortuosity is estimated empirically. As shown Eq. (31), the relative permeability of each phase is evaluated by the Stone three-phase model (Fayers and Matthews, 1984; Yang et al., 2007), and the water−oil relative permeability and liquid−gas relative permeability are given in Fig. 8. The data are partially obtained from the actual field and also refer to the relevant data of the shale reservoir in the published literature (Tian et al., 2021). Due to few experimental parameters about stress sensitivity in shale rock, this paper adopts the data from the published literature (Zhao X.R. et al., 2023).

$$K_{ro} = K_{rocw} \left[\left(\frac{K_{row}}{K_{rocw}} + K_{rw} \right) \left(\frac{K_{rog}}{K_{rocw}} + K_{rg} \right) - K_{rw} - K_{rg} \right] \quad (31)$$

where K_{rocw} refers to the oil relative permeability in the water−oil system at irreducible water saturation; K_{row} and K_{rw} are the oil and water relative permeability in the water−oil system; K_{rog} and K_{rg} are the liquid and gas relative permeability in the liquid−gas system; the values of the above parameters can be obtained from Fig. 8 according to the interpolation method.

Fig. 9 reports the matrix permeability loss under pressure sensitivity. As the reservoir pressure drops to 10 MPa (BHP value in Table 2), the permeability of the grid decreases from 0.01 to 0.0029 mD, and the permeability loss reaches 71%, which significantly impacts the long-term production of this reservoir.

Fig. 10 reports the cumulative oil production curves considering single factor and multi-mechanism coupling after 10 years. The subcase marked 'base' refers to not considering any mechanism above, and the subcase marked 'both' refers to considering all the mechanisms proposed in this paper. Others mark 'Diff,' 'S-S,' and 'N-C' as the subcase considering molecular diffusion, stress sensitivity, and the N-C effect separately. Compared with the 'base' subcase, the N-C effect significantly increases the cumulative oil production by 6.76%, while the production decreases by 4.30% after considering

Table 2
Basic reservoir and production parameters in this case.

Parameter type	Parameter	Value
Gridding parameter	Mesh size, m × m × m	20 × 10 × 20
	Mesh number	75 × 100 × 2
Reservoir and production parameter	Reservoir initial pressure, MPa	37
	Reservoir temperature, °C	135
	Irreducible water saturation	0.3
	Irreducible oil saturation	0.1
	Irreducible gas saturation	0.1
	Matrix permeability, mD	0.01
	Fracture permeability, mD	3000
	Matrix porosity, %	10
	Fracture porosity, %	50
	Fracture width, m	0.003
	Rock compressibility, bar^{-1}	1E-5
	Injection gas rate, m^3/day	1.728×10^4
	BHP, MPa	10
	tortuosity	2
	Confining stress, MPa	37
	Maximum effective stress, MPa	80
	Biot's constant	1
	Reference permeability, mD	0.01
	Surface roughness constant	1
	Average pore size, nm	20

(a) Water–oil relative permeability
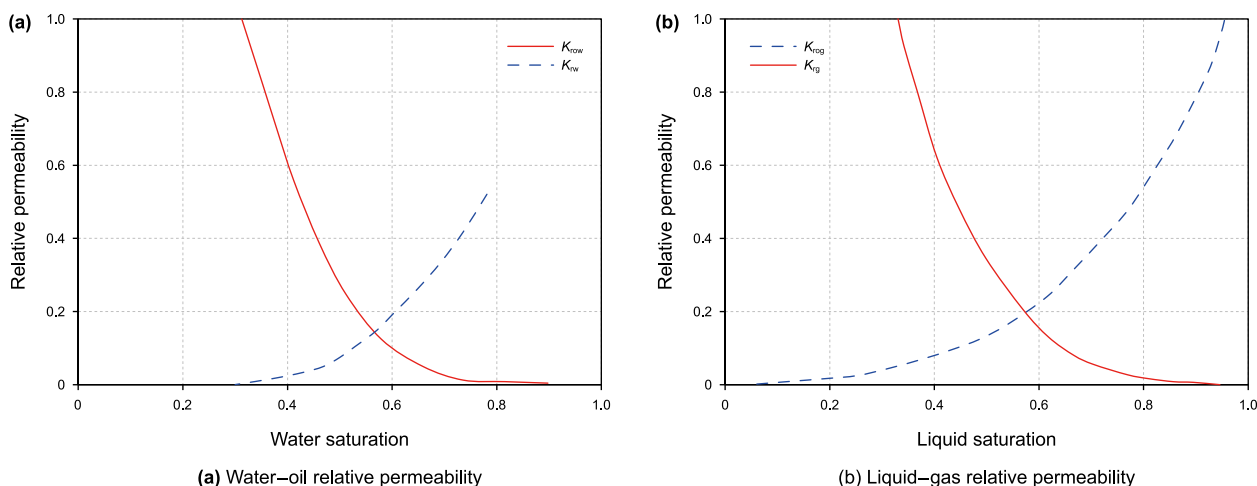
(b) Liquid–gas relative permeability

Fig. 8. Relative permeability between phases.
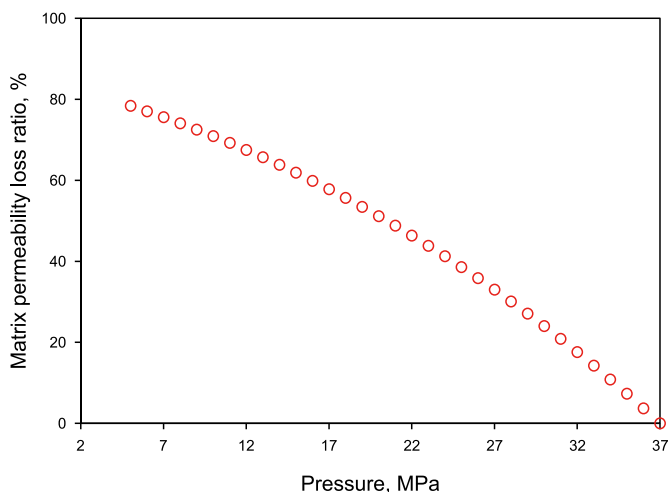
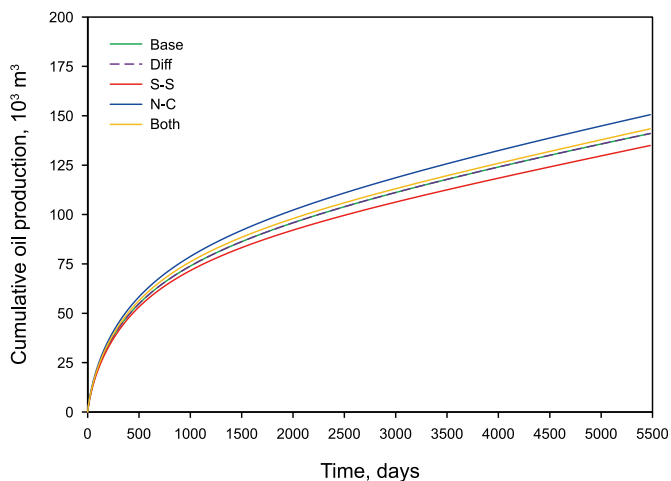**Fig. 9.** Matrix permeability loss with pressure considering stress sensitivity.
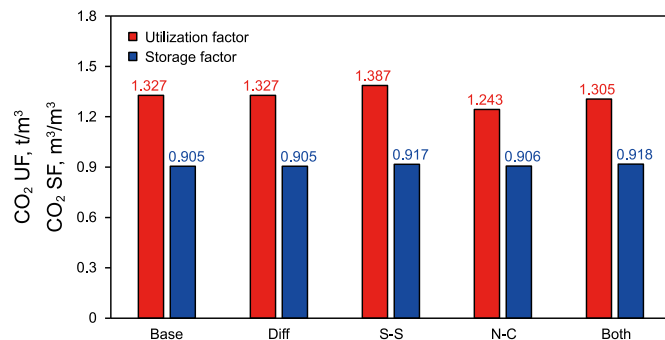

Fig. 11. Values of CO_2 UF and CO_2 SR considering different mechanisms after 15 years.

stress sensitivity. In shale gas reservoirs, molecular diffusion, as the main migration type of the gas phase, provides considerable gas production during the production period. Although the M−S approach has modeled the molecular diffusion of gas and liquid phases in shale oil reservoirs, the molecular diffusion has a minor effect on cumulative oil production, which may be related to the low diffusion coefficient of the liquid phase, and the gas phase only exists in the SRV region. The molecular diffusion may be over-estimated in shale oil reservoirs, but this conclusion needs to be further confirmed under other development methods, such as gas injection huff and puff. The interactions between mechanisms will further affect production performance. The cumulative oil production still increases by 1.66% when considering multi-mechanism coupling. It is very important to evaluate and model each mechanism reasonably.

Fig. 11 reports values of CO_2 utilization factor (CO_2 UF) and CO_2 storage factor (CO_2 SR), considering different mechanisms after 15 years. The parameters are calculated by the following equations (Eqs. (32) and (33)). CO_2 UF and CO_2 SR are important evaluated parameters for CO_2 storage capacity and CO_2-EOR (Kulkarni and Rao, 2004). CO_2 UF is the ratio of injection CO_2 mass to the production oil volume at the surface condition. CO_2 SR is the effective storage ratio, equal to the ratio of the CO_2 volume captured by the formation to the injection volume at the reservoir condition.

Fig. 10. Cumulative oil production curves considering different mechanisms during 15 years.

$$U_{CO_2 \text{ UF}} = m_{CO_2} \Big/ I_{oil}^{SC} \qquad (32)$$

$$U_{CO_2 \text{ SR}} = \left(I_{CO_2}^{RC} - N_{CO_2}^{RC} \right) \Big/ I_{CO_2}^{RC} \qquad (33)$$

where superscripts RC, SC refer to the reservoir and surface conditions, respectively; I_{CO_2} is the injection gas volume, m^3; N_{oil} is the cumulative production volume of oil, m^3; m_{CO_2} is the mass of injection CO_2, t.

The value of CO_2 UF is mainly affected by the cumulative oil production and changes linearly with the cumulative oil production, the subcase considering separately the N-C effect has the lowest CO_2 UF (1.243 t/m^3). The subcase considering separately the S-S has the lowest value (1.387 t/m^3 CO_2 UF). These evaluation parameter differences are minor when considering diffusion due to minor differences in cumulative oil production. CO_2 SR is both affected by cumulative oil production and gas phase content. The N-C effect reduces the bubble point and delays gas escape, considering the N-C effect and S-S, the subcases have the highest CO_2 SR (with 0.918 m^3/m^3).

These evaluation parameters are also affected by current reservoir conditions and production parameters, such as permeability, formation pressure, and well pattern. Sensitivity analysis was reported in subsequent studies to evaluate the change rate.

4. Results and analysis

This section performs the sensitivity analysis of fracture and production parameters to evaluate the production and CO_2 storage potential, including bottom hole pressure (BHP), injection gas rate, well spacing, and row spacing. The basic parameters and reservoir model are consistent with Section 3.2.

4.1. BHP

The effect of BHP on CO_2 storage and production is evaluated. Due to the dramatic change in composition within the SRV region, BHP is not set higher than the bubble point pressure of the initial reservoir composition. BHP is set to 15, 20, and 25 MPa. Fig. 12

reports the formation pressure and CO_2 mole fraction profiles after 15 years. The higher the BHP of the production well, the shallower the color of the SRV region. The pressure near the injection
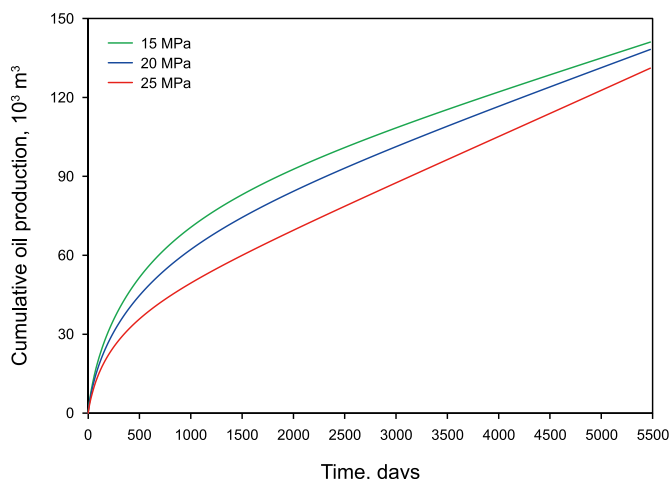

Fig. 13. Cumulative oil production curves at different BHP during 15 years.
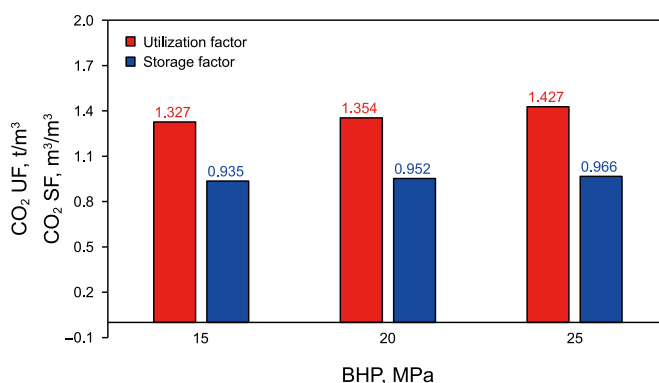

Fig. 14. Values of CO_2 UF and CO_2 SR at different BHP after 15 years.

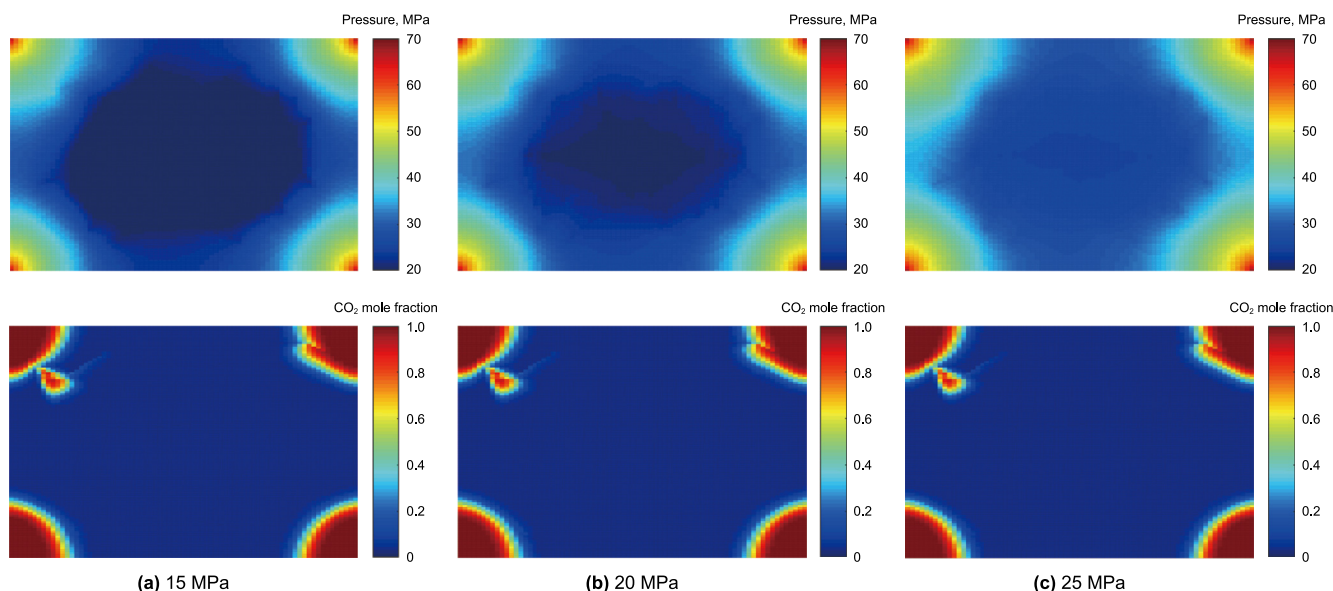**(a)** 15 MPa   **(b)** 20 MPa   **(c)** 25 MPa

Fig. 12. Pressure and CO_2 mole fraction profiles at different BHP after 15 years.

well reaches 70 MPa. The difference in CO_2 mole fraction profiles at different BHP is slight, and the irregular shape is due to the influence of natural fractures.

Fig. 13 reports the cumulative oil production at different BHP. When the constant BHP in the case decreases from 25 to 20 and 15 MPa, respectively, the recovery increases by 5.42% and 7.56%. With the increase in production time, the gap of cumulative oil production under different BHP is narrowed, indicating that the influence of N-C effect is two-sided. Although the N-C effect increases production, it will lead to the greater pressure drop in SRV region, which aggravates stress sensitivity.

As shown in Fig. 14, CO_2 UF decreases from 1.427 to 1.354 and 1.327, and CO_2 SR decreases from 0.966 to 0.952 and 0.935. In this process, gas invasion is not captured. The CO_2 production is derived from the initial reservoir fluid and can be re-injected into the formation to increase the CO_2 SR further.

4.2. Injection gas rate

Fig. 15 reports the pressure and CO_2 mole fraction profiles under different gas injection rates. High injection rates can easily lead to high formation pressure near injection wells. When the injection rate is 34,560 m^3/day, the formation pressure near the injection well reaches 90 MPa, which may cause the current formation pressure to be higher than the formation fracture pressure or excessive ground equipment load. At the same time, the gas loss may increase when the fractures communicate with the overlying strata, but this condition is not considered in this article. With the increase in injection rate, CO_2 displaces the oil near-well matrix and gradually advances to the horizontal well. The effects of fractures are clearly observed through irregular CO_2 profile changes. The CO_2 injection rate can be adjusted flexibly to adapt to the change in injection well pressure.

Fig. 16 reports the cumulative oil production with different gas injection rates. The development period is divided into the response stage (the first stage) and yield-increasing stage (the second stage). The difference between the injection rate and cumulative oil production was not observed in the first stage. Although the high injection rate maintains abnormally high pressure near the injection well, this condition does not immediately

affect the production rate of horizontal wells because pressure waves propagate more slowly in ultra-tight reservoirs. This
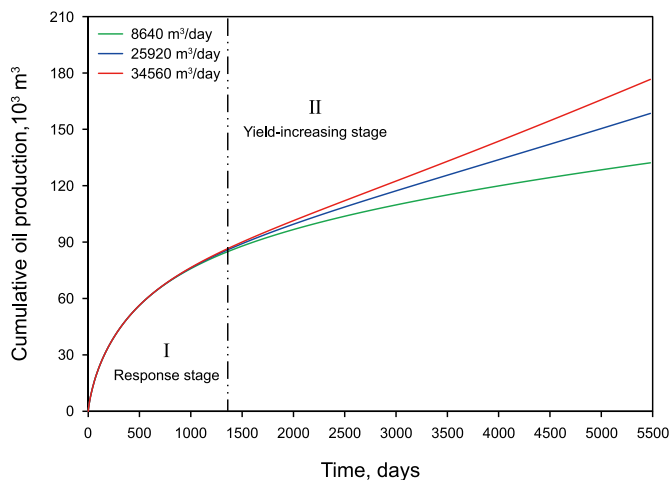

Fig. 16. Cumulative oil production curves with different injection gas rates during 15 years.
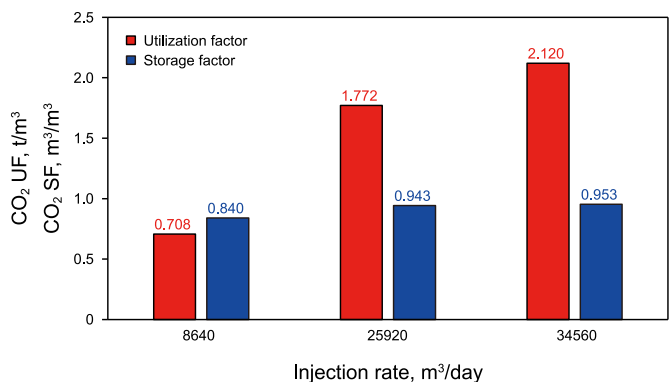

Fig. 17. Values of CO_2 UF and CO_2 SR with different injection gas rates after 15 years.

(a) 8640 m^3/day   (b) 25920 m^3/day   (c) 34560 m^3/day
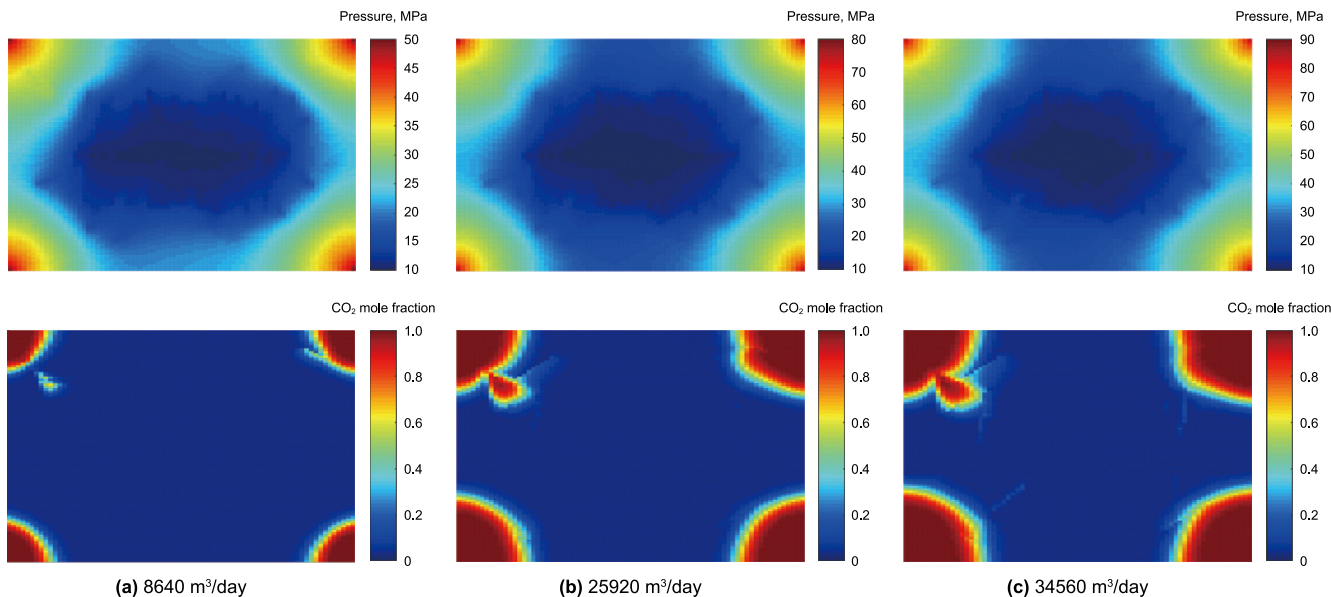
Fig. 15. Pressure and CO_2 mole fraction profiles with different injection gas rates after 15 years.

condition changes after 2000 days, and the higher gas injection rate significantly increases the cumulative oil production. The production with an injection rate of 34560 m^3/day increased by 33.57% compared to the rate of 8640 m^3/day after 15 years, and this proportion continues to increase. The return rate of a high injection rate gradually increases during the long-term production process. The reservoir properties, well pattern density, and injection parameters affect the first stage's duration.

As shown in Fig. 17, the injection rate was positively correlated with CO_2 UF and CO_2 SR. When the injection rate increased from 8640 to 25,920 and 34560 m^3/day, the CO_2 UF increased from 0.708 to 1.772 and 2.120, the CO_2 SR increased from 0.840 to 0.943 and 0.953.

4.3. Well spacing

The well spacing is the distance between injection wells. Fig. 18 reports the pressure and CO_2 mole fraction profiles under different well spacing. The well spacing is set to 375, 750, and 1500 m. The formation pressure near the SRV area is obviously uplifted. The smaller the well spacing, the smaller the range of the dark area in the pressure profile, and the larger the pressure uplift area. At the same time, the well density increases, and the CO_2 storage capacity also increases. The gas migrates rapidly along the fracture to the SRV area, and the risk of gas invasion increases sharply.

Fig. 19 reports the cumulative oil production with injection well spacing. Similarly, the two stages can still be clearly observed throughout the process. The production with injection well spacing of 375 m increases by 10.94% and 24.20% compared to well spacing of 750 and 1500 m after 15 years. As shown in Fig. 20, with the decrease in well spacing, CO_2 UF gradually increases. However, the linear change rule of CO_2 SR did not capture, which increases from 0.918 to 0.931 and decreases to 0.910, indicating the severe gas invasion at the bottom of the well. The injected CO_2 flows rapidly to the production well along the dominant channel, as shown in Fig. 18(a). A reasonable adjustment of the production system is necessary after this situation occurs.

4.4. Row spacing

Row spacing is the vertical distance between a row of injection

wells and a row of production wells. Fig. 21 reports the pressure and CO_2 mole fraction profiles under different row spacing. Row spacing is set at 200, 300, and 400 m. When the distance is reduced from 400 to 200 m, the gas flow range becomes large, the dark red
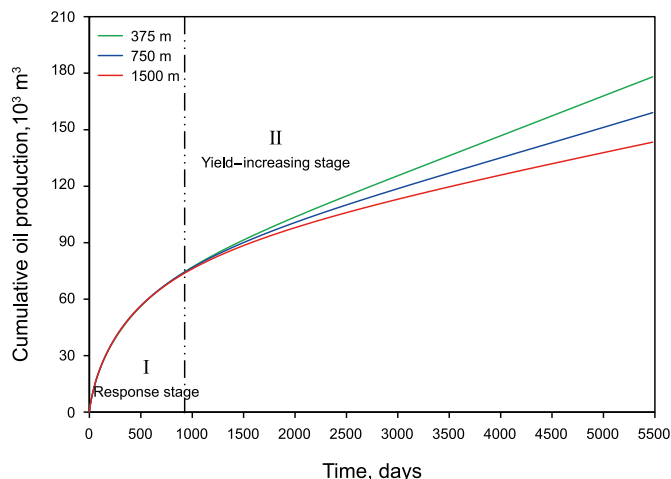

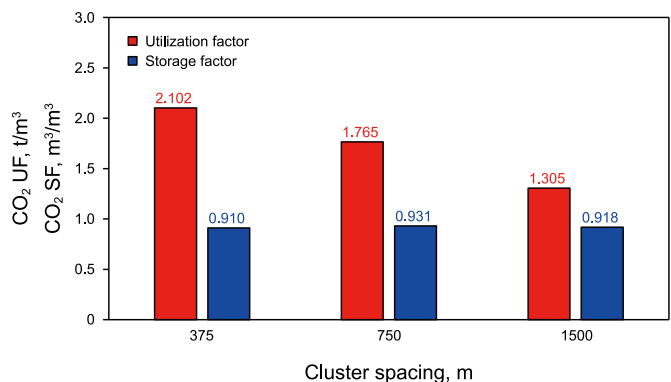**Fig. 19.** Cumulative oil production curves with different well spacing during 15 years.

Fig. 20. Values of CO_2 UF and CO_2 SR with different cluster spacing after 15 years.

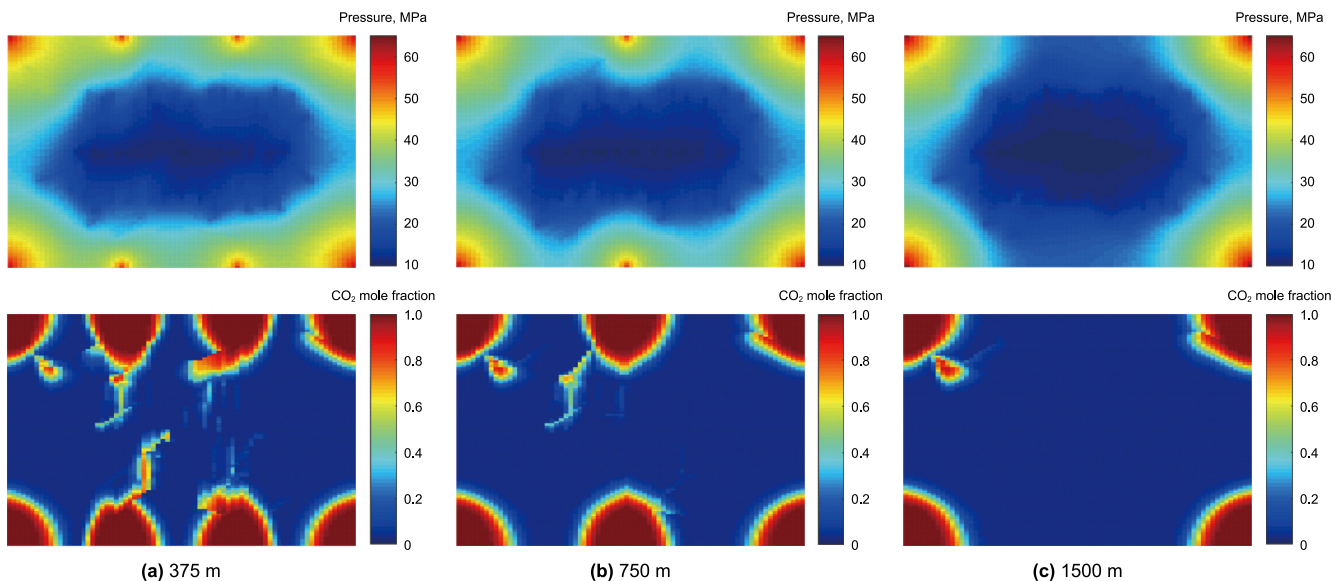**(a)** 375 m   **(b)** 750 m   **(c)** 1500 m

Fig. 18. Pressure and CO_2 mole fraction profiles with different well spacing after 15 years.
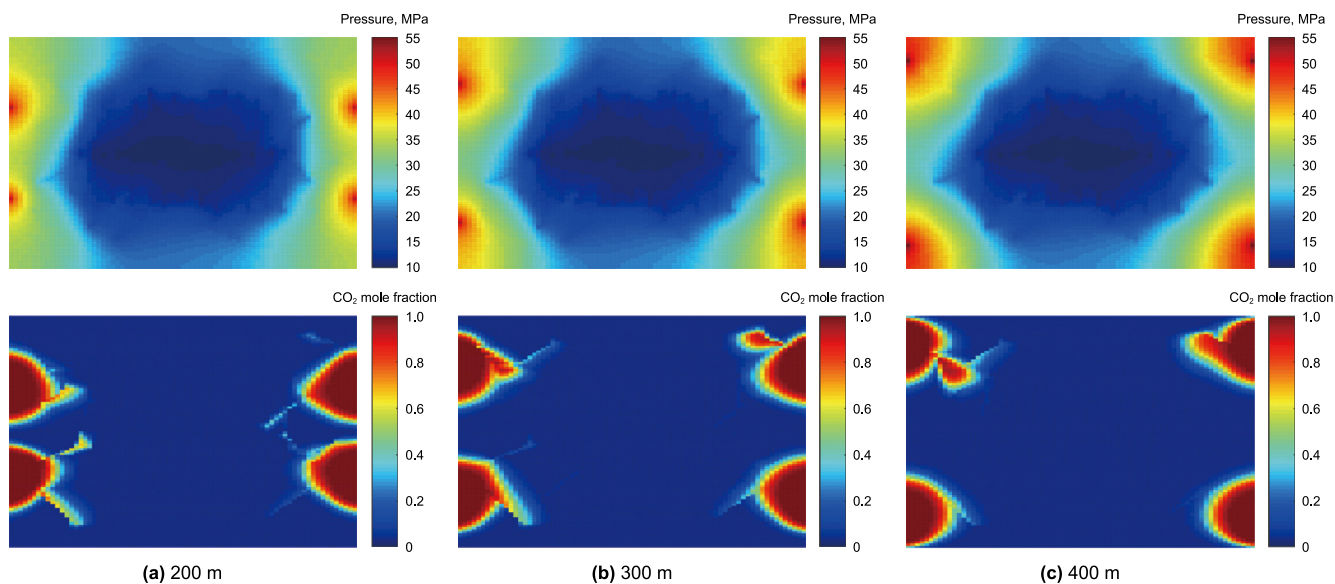
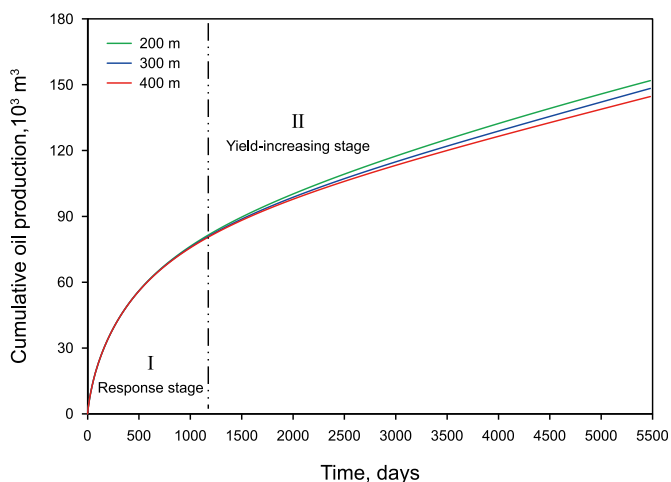**Fig. 21.** Pressure and CO_2 mole fraction profiles with different row spacing after 15 years.

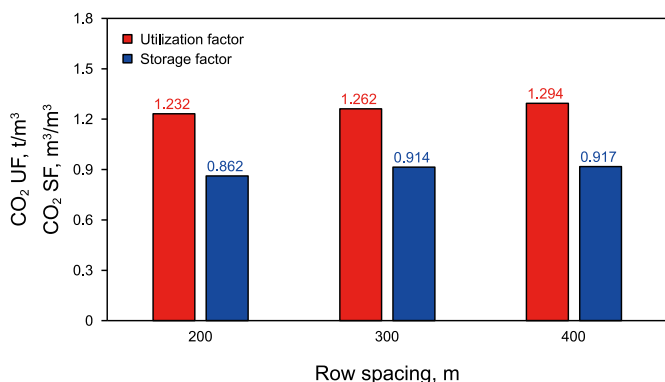**Fig. 22.** Cumulative oil production curves with different row spacing during 15 years.

Fig. 23. Values of CO_2 UF and CO_2 SR with different raw spacing after 15 years.

Fig. 24. Factors affecting cumulative oil production, blue and red represent positive and negative correlations.

area becomes shallow, and the high-pressure area near the injection well decreases.

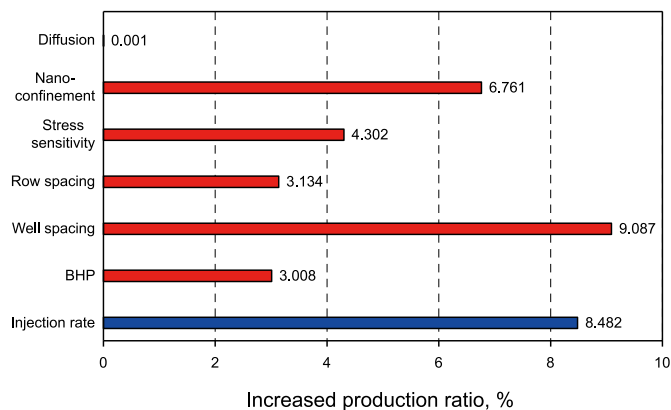Fig. 22 is the cumulative oil production with different row spacing. The cumulative oil production increases by 2.40% and 5.01% when the row spacing is reduced from 400 to 300 and 200 m. Compared with the well spacing, the row spacing has less influence on the production. However, too close row spacing is more likely to lead to gas invasion, and formation fracture in high-pressure environments will aggravate this risk. Fig. 23 shows that CO_2 UF and CO_2 SR decrease gradually with the decrease of row spacing.

4.5. Comparison of sensitivity analysis

In this section, based on the above sensitivity analysis, the main control factors for production are evaluated at a constant injection rate for 15 years. The parameters in Table 2 are used as reference values. The production and gas injection parameters (row spacing, well spacing, BHP, injection rate) were increased by the same multiple to observe production change. Eq. (34) is used to calculate the dimensionless rate of increase, and the effect of the mechanisms on production (diffusion, N-C effect, stress sensitivity) only compares the rate of increase between the mechanisms considered alone and not, date from section 3.2. As shown in Fig. 24, for parameters controlled by the production scheme, the well spacing is the main factor affecting the production, followed by the injection

rate, row spacing, and BHP. In ultra-tight shale reservoirs, too low BHP after considering stress sensitivity may significantly affect the long-term development of reservoirs. For physical properties of the reservoirs, the pore structure distribution is the main factor affecting the production, the N-C effect can significantly increase oil production, followed by stress sensitivity with a negative correlation. Due to reservoir type and oil composition, the diffusion effect is very slight, and the results are consistent with the previous study (Olorode et al., 2021). However, when multiple mechanisms are coupled, this effect may be offset due to the interaction between the mechanisms.

$$\varepsilon = \frac{\left| Q_c - Q_{\text{ref}} \right|}{e_c / e_{\text{ref}}} \qquad (34)$$

where ε is the dimensionless incremental production factor; Q_{ref} and Q_c are the cumulative oil production at the current and specified reference values of the parameter; e_c and e_{ref} are the current and reference values.

5. Conclusions

This paper proposes a multi-component numerical simulation model to evaluate the CO_2-EOR and CO_2 storage process. The report emphasizes the advantages and potential risks of CO_2 flooding. The sensitivity analysis of production and reservoir parameters provides a favorable direction for the subsequent development project. The theoretical pilot study of this paper provides the basis for the cluster and structured application of CCUS in the reservoir industry. The main conclusions of the paper are as follows.

(1) This paper develops a full multi-component numerical simulation model coupled with multi-mechanism, such as M−S diffusion, stress sensitivity, and the N-C effect. The hydraulic and natural fractures are modeled by pEDFM. The model can effectively evaluate production performance and CO_2 storage.

(2) When the N-C effect and stress sensitivity are considered alone, the production changes are 6.76% and −4.30% after 15 years. The molecular diffusion has a minor effect on oil production when the matrix permeability is 0.01 mD. The interaction between the mechanisms leads to more complex production performance. The cumulative oil production is increased by 1.66% when coupling multiple mechanisms.

(3) CO_2 UF and CO_2 SR are evaluated during CO_2-EOR process. At a constant injection rate, the CO_2 UF and CO_2 SR variation trends show a linear negative relationship with oil production.

(4) Given the well pattern in this paper, the CO_2 storage process is divided into two stages. In the first stage, the response stage, the production parameters slightly influence the oil production due to the slow propagation speed of the pressure wave in the ultra-tight reservoirs. The second stage is the yield-increasing stage, where production parameters significantly affect oil production and become more significant with the longer production time.

(5) The sensitivity analysis shows that well spacing, injection rate, and N-C effects are critical factors, but this conclusion may differ under different reservoir types and compositions.

(6) The fractures are important and the gas flows along the fractures, thus reducing the sweep range of the gas injection. Monitoring fracture development is important to prevent the risk of gas invasion, especially in ultra-tight shale reservoirs.

CRediT authorship contribution statement

Yuan-Zheng Wang: Writing − review & editing, Writing − original draft, Software. **Ren-Yi Cao:** Funding acquisition. **Zhi-Hao Jia:** Validation. **Bin-Yu Wang:** Investigation, Formal analysis. **Ming Ma:** Resources, Formal analysis. **Lin-Song Cheng:** Supervision, Project administration, Conceptualization.

Declaration of competing interest

The authors declare that they have no known competing financial interests or personal relationships that could have appeared to influence the work reported in this paper.

Acknowledgments

References

Adamson, A.W., 1990. Physical Chemistry of Surfaces, Fifth ed. John Wiley & Sons, New York City. https://doi.org/10.1149/1.2133374.

Bao, J., Tsau, J.S., Barati, R., 2018. Role of molecular diffusion in heterogeneous, naturally fractured shale reservoirs during CO_2 huff-n-puff. J. Petrol. Sci. Eng. 164, 31–42. https://doi.org/10.1016/j.petrol.2018.01.032.

Bui, M., Adjiman, C.S., Bardow, A., et al., 2018. Carbon capture and storage (CCS): the way forward. Energy Environ. Sci. 11 (5), 1062–1176. https://doi.org/10.1039/c7ee02342a.

Cao, R.Y., Fang, S.D., Jia, P., et al., 2019. An efficient embedded discrete-fracture model for 2D anisotropic reservoir simulation. J. Petrol. Sci. Eng. 174, 115–130. https://doi.org/10.1016/j.petrol.2018.11.004.

Chi, J., Ju, B.S., Lyu, G.Z., et al., 2017. A computational method of critical well spacing of CO_2 miscible and immiscible concurrent flooding. Petrol. Explor. Dev. 44 (5), 815–823. https://doi.org/10.1016/S1876-3804(17)30092-7.

Curtis, J.B., 2002. Fractured shale-gas systems. AAPG (Am. Assoc. Pet. Geol.) Bull. 86 (11), 1921–1938. https://doi.org/10.1306/61EEDDBE-173E-11D7-8645000102C1865D.

Eyinla, D.S., Leggett, S., Badrouchi, F., et al., 2023. A comprehensive review of the potential of rock properties alteration during CO_2 injection for EOR and storage. Fuel 353, 129219. https://doi.org/10.1016/j.fuel.2023.129219.

Fayers, F.J., Matthews, J.D., 1984. Evaluation of normalized Stone's methods for estimating three-phase relative permeabilities. SPE J. 24 (2), 224–232. https://doi.org/10.2118/11277-PA.

Fragoso, A., Selvan, K., Aguilera, R., 2018. An investigation on the feasibility of combined refracturing of horizontal wells and huff and puff gas injection for improving oil recovery from shale petroleum reservoirs. In: The SPE Improved Oil Recovery Conference. https://doi.org/10.2118/190284-MS.

Fuller, E.N., Schettler, P.D., Giddings, J.C., 1966. A new method for prediction of binary gas-phase diffusion coefficients. Ind. Eng. Chem. 58 (10), 18–27. https://doi.org/10.1016/0042-207X(66)90400-3.

Fuller, E.N., Ensley, K., Giddings, J.C., 1969. Diffusion of halogenated hydrocarbons in helium. the effect of structure on collision cross sections. J. Phys. Chem. 73 (11), 3678–3685. https://doi.org/10.1021/j100845a020.

Gangi, A.F., 1978. Variation of whole and fractured porous rock permeability with confining pressure. Int. J. Rock Mech. Min. Sci. Geomech. Abstracts 15 (5), 249–257. https://doi.org/10.1016/0148-9062(78)90957-9.

Hashemi, S.M.H., Sedaee, B., 2022. Mechanistic simulation of fracture effects on miscible CO_2 injection. Pet. Res. 7 (4), 437–447. https://doi.org/10.1016/j.ptlrs.2022.01.006.

Hui, M.H.R., Mallison, B., Fyrozjaee, H.M., et al., 2013. The upscaling of discrete fracture models for faster, coarse-scale simulations of IOR and EOR processes for fractured reservoirs. In: SPE Annual Technical Conference and Exhibition. https://doi.org/10.2118/166075-MS.

Huron, M.J., Vidal, J., 1979. New mixing rules in simple equations of state for representing vapour-liquid equilibria of strongly non-ideal mixtures. Fluid Phase Equil. 3, 255–271. https://doi.org/10.1016/0378-3812(79)80001-1.

ICF International, 2010. Defining CCS Ready: an Approach to an International Definition.

IEA, 2017. Energy Technology Perspectives 2017-Catalysing Energy Technology Transformations.

IEA, 2020. CCUS in Clean Energy Transitions. International Energy Agency.

IEA, 2021. An Energy Sector Roadmap to Carbon Neutrality in China. International Energy Agency.

Jia, B., Tsau, J.S., Barati, R., 2019. A review of the current progress of CO_2 injection EOR and carbon storage in shale oil reservoirs. Fuel 236, 404–427. https://doi.org/10.1016/j.fuel.2018.08.103.

Jia, Z.H., Cheng, L.S., Feng, H.R., et al., 2023. Full composition numerical simulation of CO_2 utilization process in shale reservoir using projection-based embedded discrete fracture model (pEDFM) considering N-C effect. Gas Sci. Eng. 111, 204932. https://doi.org/10.1016/j.jgsce.2023.204932.

Jiang, J., Younis, R.M., 2017. An improved projection-based embedded discrete fracture model (pEDFM) for multiphase flow in fractured reservoirs. Adv. Water Resour. 109, 267–289. https://doi.org/10.1016/j.advwatres.2017.09.017.

Khanal, A., Khoshghadam, M., Jha, H.S., et al., 2021. Understanding the effect of nanopores on flow behavior and production performance of Liquid-rich shale reservoirs. In: SPE/AAPG/SEG Unconventional Resources Technology Conference. https://doi.org/10.15530/urtec-2021-5169.

Kulkarni, M.M., Rao, D.N., 2004. Experimental investigation of various methods of tertiary gas injection. In: The SPE Annual Technical Conference and Exhibition. https://doi.org/10.2118/90589-MS.

Leahy-Dios, A., Firoozabadi, A., 2007. Unified model for nonideal multi-component molecular diffusion coefficients. AIChE J. 53 (11), 2932–2939. https://doi.org/10.1002/aic.11279.

Li, L., Lee, S.H., 2008. Efficient field-scale simulation of black oil in a naturally fractured reservoir through discrete fracture networks and homogenized media. SPE Reservoir Eval. Eng. 11 (4), 750–758. https://doi.org/10.2118/103901-PA.

Lindeloff, N., Michelsen, L.M., 2003. Phase envelope calculations for Hydrocarbon-water mixtures. SPE J. 8 (3), 298–303. https://doi.org/10.2118/85971-PA.

Lohrenz, J., Bray, B.G., Clark, C.R., 1964. Calculating viscosities of reservoir fluids from their compositions. J. Petrol. Technol. 16 (10), 1171–1176. https://doi.org/10.2118/915-PA.

Luo, P., Luo, W.G., Li, S., 2017. Effectiveness of miscible and immiscible gas flooding in recovering tight oil from Bakken reservoirs in Saskatchewan, Canada. Fuel 208, 626–636. https://doi.org/10.1016/j.fuel.2017.07.044.

Ma, X.H., 2018. Enrichment laws and scale effective development of shale gas in the southern Sichuan Basin. Nat. Gas. Ind. B. 6 (3), 240–249. https://doi.org/10.1016/j.ngib.2018.10.005.

Moinfar, A., Varavei, A., Sepehrnoori, K., et al., 2014. Development of an efficient embedded discrete fracture model for 3D compositional reservoir simulation in fractured reservoirs. SPE J. 19 (2), 289–303. https://doi.org/10.2118/154246-PA.

Moortgat, J., Firoozabadi, A., 2013. Fickian diffusion in Discrete-fractured media from chemical potential gradients and comparison to experiment. Energy Fuels 27, 5793–5805. https://doi.org/10.1021/ef401141q.

Morishige, K., Fujii, H., Uga, M., et al., 1997. Capillary critical point of argon, nitrogen, oxygen, ethylene, and carbon dioxide in MCM-41. Langmuir 13 (13), 3494–3498. https://doi.org/10.1021/la970079u.

Olorode, O., Wang, B., Rashid, H.U., 2020. Three-dimensional projection-based embedded discrete-fracture model for compositional simulation of fractured reservoirs. SPE J. 25 (4), 2143–2161. https://doi.org/10.2118/201243-PA.

Olorode, O., Amer, H., Rashid, H.U., 2021. The role of diffusion in primary and enhanced oil recovery from fractured unconventional reservoirs. In: SPE/AAPG/SEG Asia Pacific Unconventional Resources Technology Conference. https://doi.org/10.15530/AP-URTEC-2021-208387.

Rachford, H.H., Rice, J.D., 1952. Procedure for use of electrical digital computers in calculating flash vaporization hydrocarbon equilibrium. JPT 4 (10), 19. https://doi.org/10.2118/952327-G.

Rao, X., Cheng, L.S., Cao, R.Y., et al., 2020. A modified projection-based embedded discrete fracture model (pEDFM) for practical and accurate numerical simulation of fractured reservoir. J. Petrol. Sci. Eng. 187, 106852. https://doi.org/10.1016/j.petrol.2019.106852.

Rao, X., Xin, L.Y., He, Y.X., et al., 2022. Numerical simulation of two-phase heat and mass transfer in fractured reservoirs based on projection-based embedded discrete fracture model (pEDFM). J. Petrol. Sci. Eng. 208, 109323. https://doi.org/10.1016/j.petrol.2021.109323.

Sanaei, A., Jamili, A., Callard, J., 2014. Effect of pore size distribution and connectivity on phase behavior and gas condensate production from unconventional resources. In: SPE Unconventional Resources Conference. https://doi.org/10.2118/168970-MS.

Sanchez-Rivera, D., Mohanty, K., Balhoff, M., 2015. Reservoir simulation and optimization of Huff-and-Puff operations in the Bakken shale. Fuel 147, 82–94. https://doi.org/10.1016/j.fuel.2014.12.062.

Sandve, T.H., Berre, I., Nordbotten, J.M., 2012. An efficient multi-point flux approximation method for discrete fracture–matrix simulations. J. Comput. Phys. 231 (9), 3784–3800. https://doi.org/10.1016/j.jcp.2012.01.023.

Singh, S.K., Singh, J.K., 2011. Effect of pore morphology on vapor–liquid phase transition and crossover behavior of critical properties from 3D to 2D. Fluid Phase Equil. 300 (1–2), 182–187. https://doi.org/10.1016/j.fluid.2010.10.014.

Singh, S.K., Sinha, A., Deo, G., et al., 2009. Vapor-liquid phase coexistence, critical properties, and surface tension of confined alkanes. J. Phys. Chem. 113 (17), 7170–7180. https://doi:10.1021/jp8073915.

Song, Y.L., Gu, S.H., Song, Z.J., 2020a. Effect of confinement on the three-phase equilibrium of water-oil-CO_2 mixtures in nanopores. Petrol. Sci. 19 (1),

203–210. https://doi.org/10.2118/191547-MS.

Song, Y.L., Song, Z., Feng, D., et al., 2020b. Phase behavior of hydrocarbon mixture in shale nanopores considering the effect of adsorption and its induced critical shifts. Ind. Eng. Chem. Res. 59 (17). https://doi.org/10.1021/acs.iecr.0c00490.

Song, Z.J., Song, Y.L., Guo, Y.L., et al., 2020. Adsorption induced critical shifts of confined fluids in shale nanopores. Chem. Eng. J. 385, 123837. https://doi.org/10.1016/j.cej.2019.123837.

Steven, B.H., Charles, D.G., James, A.S., et al., 2013. Hydrocarbon mobilization mechanisms from upper, middle, and lower Bakken reservoir rocks exposed to CO_2. In: SPE Unconventional Resources Conference. https://doi.org/10.2118/167200-MS.

Sun, L.D., Liu, H., He, W.Y., et al., 2021. An analysis of major scientific problems and research paths of Gulong shale oil in Daqing Oilfield, NE China. Petrol. Explor. Dev. 48 (3). https://doi.org/10.11698/PED.2021.03.02.

Sun, L.D., Cui, B.W., Zhu, R.K., et al., 2023. Shale oil enrichment evaluation and production law in Gulong Sag, Songliao Basin, NE China. Petrol. Explor. Dev. 50 (3). https://doi.org/10.11698/PED.20230178.

Ţene, M., Bosma, S.B.M., Kobaisi, M.S.A., et al., 2017. Projection-based embedded discrete fracture model (pEDFM). Adv. Water Resour. 105, 205–216. https://doi.org/10.1016/j.advwatres.2017.05.009.

Tian, Y., Zhang, C., Lei, Z.D., et al., 2021. An improved multicomponent diffusion model for compositional simulation of fractured unconventional reservoirs. SPE J. 26 (5), 3316–3341. https://doi.org/10.2118/204010-PA.

Vignes, A., 1966. Diffusion in binary mixtures. Ind. Eng. Chem. Fund. 5 (2), 189–199. https://doi.org/10.1021/i160018a007.

Wan, T., Zhang, J., Dong, Y., 2023. The impact of fracture network on CO_2 storage in shale oil reservoirs. Geoenergy Sci. Eng. 231, 212322. https://doi.org/10.1016/j.geoen.2023.212322.

Wang, Q., Pfeiffer, H., Amal, R., et al., 2022. Introduction to CO_2 capture, utilization and storage (CCUS). React. Chem. Eng. 7 (3), 487–489. https://doi.org/10.1039/D2RE90007F.

Wang, R., 2023. Status and perspectives on CCUS clusters and hubs. Unconv. Res., 100065 https://doi.org/10.1016/j.uncres.2023.100065.

Wang, Y.Z., Cao, R.Y., Jia, Z.H., et al., 2023. Phase behavior and hydrocarbons distribution in shale oil during EOR with nano-confinement effect. Front. Energy Res. 11, 1237254. https://doi.org/10.3389/fenrg.2023.1237254.

Wasaki, A., Akkutlu, Y.I., 2015. Permeability of organic-rich shale. SPE J. 20 (6), 1384–1396. https://doi.org/10.2118/170830-PA.

Xu, Y., Cavalcante, J.S.A., Yu, W., et al., 2017. Discrete-fracture modeling of complex hydraulic-fracture geometries in reservoir simulators. SPE Reservoir Eval. Eng. 20 (2), 403–422. https://doi.org/10.2118/183647-PA.

Xu, Y.F., Yu, W., Sepehrnoori, K., 2019. Modeling dynamic behaviors of complex fractures in conventional reservoir simulators. SPE Reservoir Eval. Eng. 22 (3), 1110–1130. https://doi.org/10.2118/194498-PA.

Yang, T., Fevang, Ø., Christoffersen, K., et al., 2007. LBC viscosity modeling of gas condensate to heavy oil. In: The SPE Annual Technical Conference and Exhibition. https://doi.org/10.2118/109892-MS.

Yanze, Y., Clemens, T., 2012. The role of diffusion for nonequilibrium gas injection into a fractured reservoir. SPE Reservoir Eval. Eng. 15 (1), 60–71. https://doi.org/10.2118/142724-PA.

Yu, W., Xu, Y.F., Weijermars, R., et al., 2018. A numerical model for simulating pressure response of well interference and well performance in tight oil reservoirs with complex-fracture geometries using the fast embedded-discrete-fracture-model method. SPE Reservoir Eval. Eng. 21 (2), 489–502. https://doi.org/10.2118/184825-PA.

Zarragoicoechea, G.J., Kuz, V.A., 2004. Critical shift of confined fluid in a nanopore. Fluid Phase Equil. 220, 7–9. https://doi.org/10.1016/j.fluid.2004.02.014.

Zhang, N., Yin, M.F., Wei, M.Z., et al., 2019. Identification of CO_2 sequestration opportunities: CO_2 miscible flooding guidelines. Fuel 241, 459–467. https://doi.org/10.1016/j.fuel.2018.12.072.

Zhang, Y., Yu, W., Sepehrnoori, K., et al., 2017. A comprehensive numerical model for simulating fluid transport in nanopores. Sci. Rep. 7, 40507. https://doi.org/10.1038/srep40507.

Zhang, Z.E., Wang, T., Blunt, M.J., et al., 2020. Advances in carbon capture, utilization and storage. Appl. Energy 278, 115627. https://doi.org/10.1016/j.apenergy.2020.115627.

Zhao, F.L., Hao, H.D., Lv, G.Z., et al., 2018. Performance improvement of CO_2 flooding using production controls in 3D areal heterogeneous models: experimental and numerical simulations. J. Petrol. Sci. Eng. 164, 12–23. https://doi.org/10.1016/j.petrol.2018.01.036.

Zhao, J.Y., Fan, J.M., He, Y.H., et al., 2015. Optimization of horizontal well injection-production parameters for ultra-low permeable–tight oil production: a case from Changqing Oilfield, Ordos Basin, NW China. Petrol. Explor. Dev. 42 (1), 74–82. https://doi.org/10.1016/S1876-3804(15)60008-8.

Zhao, W.Z., Bian, C.S., Li, Y.X., et al., 2023. Enrichment factors of movable hydrocarbons in lacustrine shale oil and exploration potential of shale oil in Gulong Sag, Songliao Basin, NE China. Petrol. Explor. Dev. 50 (3), 520–533. https://doi.org/10.11698/PED20230058.

Zhao, X.R., Chen, Z.M., Wang, B., et al., 2023. A multi-medium and multi-mechanism model for CO_2 injection and storage in fractured shale gas reservoirs. Fuel 345, 128167. https://doi.org/10.1016/j.fuel.2023.128167.